

Design strong anomalous Hall effect via spin canting in antiferromagnetic nodal line materials

Congcong Le,¹ Claudia Felser,¹ and Yan Sun^{1,*}

¹Max Planck Institute for Chemical Physics of Solids, 01187 Dresden, Germany

(Dated: May 20, 2021)

The interplay between magnetism and topological electronic structure offers a large freedom to design strong anomalous Hall effect (AHE) materials. A nodal line from band inversion is a typical band structure to generate strong AHE. Whereas, in most collinear antiferromagnets (AFMs), the integration of Berry curvatures on Brillouin zone is forced to zero by the joint TO symmetry, where T and O are time reversal and a space group operation, respectively. Even with inverted band structures, such kind of AFM cannot have AHE. Therefore, so far, AFM nodal line band structures constructed by spin degenerated bands didn't get much attentions in AHE materials. In this work, we illustrate that such kind of band structure indeed provides a promising starting point to generated strong local Berry curvature by perturbations and, therefore, strong intrinsic AHE. In specific AFM compounds of $AMnBi_2$ ($A=Ca$ and Yb) with inverted band structure, we found a strong AHE induced by a weak spin canting, and due to nodal line in the band structure the anomalous Hall conductivity keeps growing as the canting angle increases. Since such spin-canting can be adjusted via doping experimentally, it provides another effective strategy to generate and manipulate strong AHE

PACS numbers: 75.85.+t, 75.10.Hk, 71.70.Ej, 71.15.Mb

I. INTRODUCTION

In recent years, materials with strong anomalous Hall effect (AHE)¹ have attracted extensive attentions in the field of materials science and condensed matter physics, which is connected to fundamental topological band structure and potential applications in electronic devices. Since the intrinsic AHE can be understood as the integral of Berry curvature in the momentum space²⁻⁴, band structures with strong Berry curvature are desired to have strong AHE. Weyl points and nodal lines are two kinds of promising band structures, which can generate strong local Berry curvature. With such guiding principle, strong AHE materials with both large anomalous Hall conductivity (AHC) and anomalous angle (AHA) were observed in ferromagnetic Weyl semimetal (WSM) $Co_3Sn_2S_2$ ⁵⁻⁷, nodal semimetal of layered ferromagnetic compound Fe_3GeTe_2 ^{8,9} and Heusler compound $Co_2Mn(Ga/Al)$ ¹⁰⁻¹⁵ et. al.

A crucial property of Berry curvature is odd under time reversal operator⁴, and hence AHE can only exist in magnetic system in linear response region. Due to broken time reversal symmetry T , the ferromagnet can host non-zero AHE. However, in the collinear antiferromagnets (AFM), though the time reversal is broken, there are two kinds of combined symmetries TO between time reversal operation T and a space group operation O , where O is a fractional translation or inversion symmetry. Then, the combined symmetry TO can also change the sign of Berry curvature, and results in the cancellation of Berry curvature when integrated over the full Brillouin zone (BZ). Therefore, AHE can only exist in a few situations without combined symmetries TO , such as non-collinear AFM in $FeMn$, NiS_2 , cubic $Mn_3(Ir/Pt)$ and hexagonal $Mn_3(Ge/Sn)$ ¹⁶⁻²², and collinear AFM Ti_2MnAl and RuO_2 ^{23,24}. On the other hand, AMF with combined symmetries TO almost did not attract much attention in AHE materials, even with nodal-line-like special band structures. Indeed, as we will show bellow, by perturbation, the nodal-line-like special band structures in the AMF materials with combined symmetries maybe generate strong AHE.

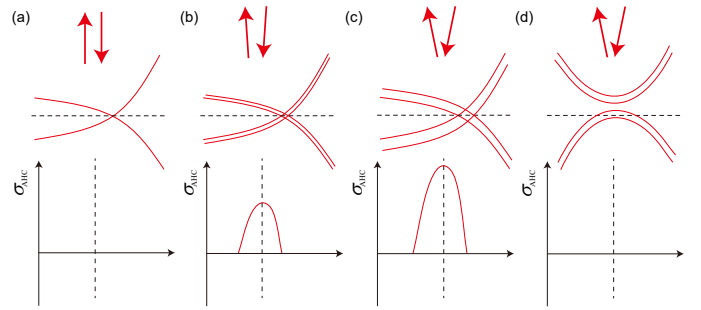


FIG. 1: (color online) Schematic of AHE in the spin canted AFM order with(a-c) and without(d) band inversion, σ_{AHC} is AHC and E_f is Fermi level. (a) The canting angle $\theta=0$. (b) The small canting angle θ . (c) The large canting angle θ . (d) AHE in the spin canted AFM order without band inversion in the large canting angle θ .

In this work, we propose an effective strategy to generate strong Berry curvature by perturbations of spin-canting based on collinear AFM nodal line band structures with combined symmetries TO . Fig.1 shows schematic of AHE in the spin canted AFM order with inverted band structure, where σ_{AHC} is AHC. At the canting angle $\theta=0$, the bands are degeneracy due to time reversal and inversion symmetries, and hence σ_{AHC} is zero, shown in Fig.1(a). When the canting angle θ is small, the two degenerate bands are split because of broken time reversal symmetry, suggesting that σ_{AHC} should be non-zero, as shown in Fig.1(b). Moreover, since the band inversion already exists in spin-degenerated bands, a type of canting can lead to a shape change of Berry curvature and AHC. When the canting angle θ becomes large, the two degenerate bands are more split, and σ_{AHC} maybe become larger, shown in Fig.1(c). However, if the canted AFMs can not host topological band structures, and their AHEs are almost zero, shown in Fig.1(d). Based on the above schematic, we perform an *ab initio* analysis for AHE as the canting angle changes in the spin canting C-type AFM materials $AMnBi_2$ ($A=Ca$ and Yb)²⁵⁻³¹, where the band inversion leads to a topological

nodal ring without considering spin-orbital coupling (SOC). We find that the AHC always keeps growing as the canting angle increases, and doping electrons can reduce AHC while doping holes strengthen AHC.

II. METHOD

Our calculations are performed using density functional theory (DFT) as implemented in the Vienna ab initio simulation package (VASP) code^{32–34}. The Perdew-Burke-Ernzerhof (PBE) exchange-correlation functional and the projector-augmented-wave (PAW) approach are used. Throughout the work, the cutoff energy is set to be 550 eV for expanding the wave functions into a plane-wave basis. The Brillouin zone is sampled in the k space within the Monkhorst-Pack scheme³⁵, and the k mesh used is $10 \times 10 \times 4$ on the basis of the equilibrium structure. In our calculations, a C-type AFM order along the c -axis, a spin-canting and SOC are included.

To calculate AHC, we project the *ab initio* DFT Bloch wave function into high symmetric atomic-orbital-like Wannier functions³⁶ with diagonal position operator, as performed in the Vienna ab initio simulation package (VASP) code^{32–34}. For obtaining precise Wannier functions, we include the outermost s - and d -orbital for Ca, d -orbital for element Mn and p -orbital for element Bi, which guarantees the full bands overlap from *ab-initio* and Wannier functions.

III. SYMMETRY ANALYSIS

The crystal structure of AMnBi_2 ($A=\text{Ca}$ and Yb) with nonsymmorphic space group $G=\text{P4/nmm}$ (No.129) is shown in Fig.2(a), where the MnBi_1 layers possess an anti-PbO-type atom arrangement and there are a square lattice sheet of Bi_2 atoms. Mn and Bi_2 atoms occupy Wyckoff positions $2a \{(0,0,0), (1/2,1/2,0)\}$ and $2b \{(0,0,1/2), (1/2,1/2,1/2)\}$ respectively, which have the same corresponding site symmetry group D_{2d} , while A and Bi_1 atoms occupy the same Wyckoff positions $2c \{(1/2,0,z), (0,1/2,-z)\}$ with corresponding site symmetry group C_{4v} . In the nonsymmorphic space group $G=\text{P4/nmm}$, the quotient group G/L is specified by 16 symmetry operations, where we denote L as the translation group with respect to the unit cell. The nonsymmorphic symmetry operations are $\tilde{C}_{2x} = \{C_{2x}|1/2, 1/2, 0\}$, $\tilde{C}_{2y} = \{C_{2y}|1/2, 1/2, 0\}$ and $\tilde{M}_{xy} = \{M_{xy}|1/2, 1/2, 0\}$ with respect to the original point at Mn site.

Since the AMnBi_2 has AFM order at Mn atoms with spins along the z axis, the following will analyze magnetic space groups and point groups. We choose Mn site as the origin, and the 16 symmetry operations operations can be specified equivalently as $D_{2d} \oplus \{I|1/2, 1/2, 0\}D_{2d}$, where I is a space inversion and the generators of D_{2d} are $C_{2,z}$, $C_{2,xy}$ and M_y . Firstly, Due to spin at Mn atoms along the z axis, $C_{2,z}$ cannot change the direction of spin while $C_{2,xy}$ and M_y flip spin, indicating that $C_{2,xy}$ and M_y are broken by AFM order at Mn atoms. Combined with time reversal symmetry T , we can get the magnetic point group $42'm'$ corresponding to

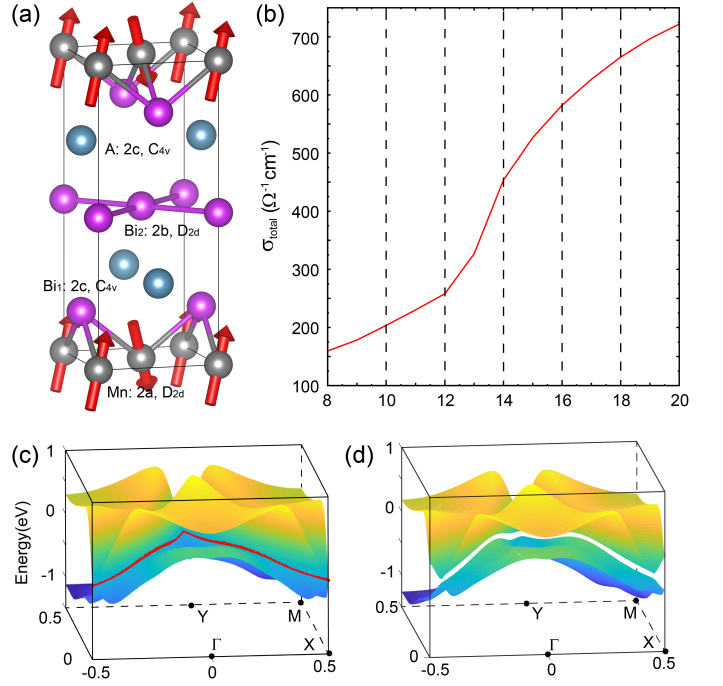


FIG. 2: (color online) (a) The crystal structure and C-type AFM order of AMnBi_2 with spin canting along the $(1,1,0)$ direction. Wyckoff positions and corresponding site symmetry group are given. (b) Canting angle dependence of the AHC σ_{AHC} in the CaMnBi_2 . (c) and (d) The band structures in the $k_z=0$ plane without and with SOC, where red line is a nodal line protected by glide plane symmetry and SOC can break the nodal line into opened gaps.

point group D_{2d} , where the generators are $C_{2,z}$, $TC_{2,xy}$ and TM_y . Secondly, Since the crystal symmetries in the $\tilde{I}D_{2d}$ with $\tilde{I} = \{I|1/2, 1/2, 0\}$ exchange Mn sublattice and inversion symmetry I can not flip spin, $C_{2,xy}$ and M_y will be maintained while $C_{2,z}$ is broken, suggesting that the magnetic generators corresponding to $\tilde{I}D_{2d}$ are $T\tilde{I}$, $T\tilde{I}C_{2,z}$, $\tilde{I}C_{2,xy}$ and $\tilde{I}M_y$. Finally, based on the above analysis, we find that the magnetic space group of AMnBi_2 with AFM order along the z axis is $P4'/n'm'm$ with magnetic point group $4'/m'm'm$. Due to $T\tilde{I}$ symmetry, the integration of Berry curvatures on BZ are forced to zero.

Since a spin canting exists in the AMnBi_2 with an in-plane ferromagnetic, and the magnitude of canting angle can be experimentally adjusted by doping³¹. We take the same canting direction $(1,1,0)$ as the papers^{30,31}, which can break $T\tilde{I}$ symmetry, indicating that AHE can exist. Then, the corresponding magnetic space group becomes $m'm2'$, where the symmetries are $\text{TC}_{2,\bar{x}y}$, M_{11} , TM_z , E, which can host non-zero AHE.

The AHC tensor can be written as

$$\sigma_{\alpha\beta}^{\gamma} = -\sum_n \frac{e^2}{\hbar} \int_{\text{BZ}} \frac{d\mathbf{k}}{(2\pi)^3} f_n(\mathbf{k}) \Omega_{n,\alpha\beta}^{\gamma}(\mathbf{k}),$$

$$\Omega_{n,\alpha\beta}^{\gamma}(\mathbf{k}) = -2 \text{Im} \langle \nabla_{\alpha} u_n(\mathbf{k}) | \nabla_{\beta} u_n(\mathbf{k}) \rangle, \quad (1)$$

Under crystal symmetry g , the relation of $\Omega_{n,\alpha\beta}^{\gamma}(\mathbf{k})$ be-

tween \mathbf{k} and $g\mathbf{k}$ is given by

$$\begin{aligned}\Omega_{n,\alpha\beta}^\gamma(g\mathbf{k}) &= -2 \text{Im} \left\langle \frac{\partial u_n(g\mathbf{k})}{\partial k_\alpha} \middle| \frac{\partial u_n(g\mathbf{k})}{\partial k_\beta} \right\rangle, \\ &= -2 \sum_{\alpha'\beta'} \text{Im} \left\langle \frac{\partial(g\mathbf{k})_{\alpha'}}{\partial \mathbf{k}_\alpha} \frac{\partial u_n(g\mathbf{k})}{\partial(g\mathbf{k})_{\alpha'}} \middle| \frac{\partial(g\mathbf{k})_{\beta'}}{\partial \mathbf{k}_\beta} \frac{\partial u_n(g\mathbf{k})}{\partial(g\mathbf{k})_{\beta'}} \right\rangle, \\ &= \sum_{\alpha'\beta'} \frac{\partial(g\mathbf{k})_{\alpha'}}{\partial \mathbf{k}_\alpha} \frac{\partial(g\mathbf{k})_{\beta'}}{\partial \mathbf{k}_\beta} \Omega_{n,\alpha'\beta'}^{\gamma'}(\mathbf{k}), \\ \Omega_{n,\alpha'\beta'}^{\gamma'}(\mathbf{k}) &= -2 \text{Im} \left\langle \frac{\partial u_n(\mathbf{k})}{\partial \mathbf{k}_{\alpha'}} \middle| \frac{\partial u_n(\mathbf{k})}{\partial \mathbf{k}_{\beta'}} \right\rangle,\end{aligned}$$

Where α' can not be equal to β' . It is clear that the AHC is invariant under inversion symmetry I , namely $\Omega_{n,\alpha\beta}^\gamma(\mathbf{k}) = \Omega_{n,\alpha\beta}^\gamma(I\mathbf{k})$. Then, we consider the constrain of the magnetic space group $m'm2'$ on AHC, where considering mirror symmetry $M_{11}(-\mathbf{k}_y, -\mathbf{k}_x, \mathbf{k}_z)$ is enough. Under mirror symmetry M_{11} , the transformation of Berry curvature $\Omega_{n,\alpha\beta}^\gamma(\mathbf{k})$ can be given by

$$\Omega_{xy}^z(\mathbf{k}) = -\Omega_{xy}^z(M_{11}\mathbf{k}), \quad \Omega_{xz}^y(\mathbf{k}) = -\Omega_{yz}^x(M_{11}\mathbf{k}), \quad (3)$$

Hence, under the constrain of magnetic space group $m'm2'$, the shape of the AHC tensors is

$$\begin{pmatrix} 0 & 0 & \sigma_{xz} \\ 0 & 0 & -\sigma_{xz} \\ -\sigma_{xz} & \sigma_{xz} & 0 \end{pmatrix}, \quad (4)$$

IV. AB INITIO ANALYSIS OF ANOMALOUS TRANSPORTS

Fig.2(c) and (d) show band structures without and with SOC in the $k_z=0$ plane, where the half of BZ ($-0.5 < k_x < 0.5$, and $0 < k_y < 0.5$) is shown for the convenience of seeing nodal line. There is a band inversion from intercalated Bi_2 $p_{x/y}$ orbitals, which lead to quasi two-dimensional band crossing. When the SOC is ignored, the crossing bands can be referred to as K and $K+Q$ bands. Similar to the symmetry analysis of iron superconductors³⁷, the K and $K+Q$ bands are the different eigenvalues of the glide plane symmetry²⁹, indicating that the nodal ring from Bi_2 $p_{x/y}$ band crossing is robust, shown in Fig.2(c). When the on-site SOC is included, the spin-flip term $\langle p_x, \sigma | H_{\text{soc}} | p_y, \bar{\sigma} \rangle$ with the spin index σ can be non-zero²⁹. Hence, the crossing bands can hybridize each other and the nodal line can be gapped, shown in Fig.2(d). In the following, we will calculate AHC and consider how does the nodal line contribute to AHC.

We calculated the AHC tensor of CaMnBi_2 with Fermi level lying at the charge neutral points, and Fig.2(b) shows canting angle dependence of the AHC σ_{AHC} with spin canting along the (1,1,0) direction, where $\sigma_{AHC} = \sqrt{\sigma_{xz}^2 + \sigma_{yz}^2} = \sqrt{2}\sigma_{xz}$ due to $\sigma_{yz} = -\sigma_{xz}$. At 8° canting angle, the AHC σ_{AHC} has a small value of $159.50 \Omega^{-1}\text{cm}^{-1}$,

whereas it is a large value of $721.90 \Omega^{-1}\text{cm}^{-1}$ at 20° canting angle. With the canting angle increasing from 8° to 20° , the AHC σ_{AHC} always keep growing, and is not saturated even if the canting angle reaches 20° . What's more, between 12° and 14° , the rate of AHC increasing is larger. To explain the variation of AHC with canting angle, we take three (8° , 13° and 18°) canting angles as examples to calculate band structures and local momentum distribution of Berry curvature in the BZ with spin canted C-type AFM states, where the magnitude of magnetic moment in the xy-plane (z-direction) are $0.53\mu_B$ ($3.81\mu_B$), $0.99\mu_B$ ($3.74\mu_B$) and $1.31\mu_B$ ($3.63\mu_B$) respectively.

Firstly, Fig.3 (a) shows band structures at 8° canting angle. Similar to band structures without canting angle³¹, near the Fermi level, the valence and conduction bands are mainly attributed to the p orbitals of the intercalated Bi_2 atoms. Because of ferromagnetic in the xy plane, the bands are split into spin-up and spin-down. The small hole pockets around the Γ point are dominated by the intercalated Bi_2 - p_z (blue) orbital, which is remarkably split due to hybridizing with Mn d orbitals; The electronic pockets from nodal line mainly originate from the intercalated Bi_2 - $p_{x/y}$ (green) orbitals, which is less sensitive to the ferromagnetic in the xy plane and is hardly split. Fig.3 (d) shows the local momentum distribution of Berry curvature in the BZ at 8° canting angle. Since the value of AHC σ_{AHC} is $159.50 \Omega^{-1}\text{cm}^{-1}$ at 8° canting angle, the total Berry curvature contributed by the hole pockets near Γ is positive and small while the total Berry curvature from electronic pockets is negative and large. The nodal line has dispersion in the BZ, which can result in electronic pockets at the fermi level, and hence the nodal line is mainly responsible for non-zero AHC.

Secondly, when the canting angle is increased to 13° , the split of band structures become more larger as the magnitude of ferromagnetic in the xy-plane increases. Then, the electronic pockets from nodal line have more splits, which maybe strengthen AHC; The Mn d-orbital bands can also attribute a hole pocket near Γ point which can result in a positive Berry curvature, shown in Fig.3 (b) and (e). Hence, the AHC of 13° canting angle becomes more greater than that of 8° , shown in Fig.2(b). Finally, when the canting angle is further increased to 18° , a big hole pocket near Γ point is completely contributed by the Mn-d orbitals due to large band splits induced by strong ferromagnetism. Then, the big hole pocket can result in a big and positive Berry curvature, indicating that the AHC of 18° canting angle becomes more larger, shown in Fig.3 (c) and (f).

Here, summarizing the above analysis. We find that the ferromagnetism in the xy plane becomes larger with the increasing of the canting angle, which can lead to greater splits of band structures. Then, the hole pocket contributed by Mn d orbitals will become larger, and can result in big and negative Berry curvature. Moreover, the electronic pockets from nodal line mainly contribute to AHC, indicating that the nodal line is responsible for non-zero AHC. As the ferromagnetism increases, the electronic pockets have more splits, which can strengthen AHC. Therefore, the AHC always keeps growing as the canting angle increases.

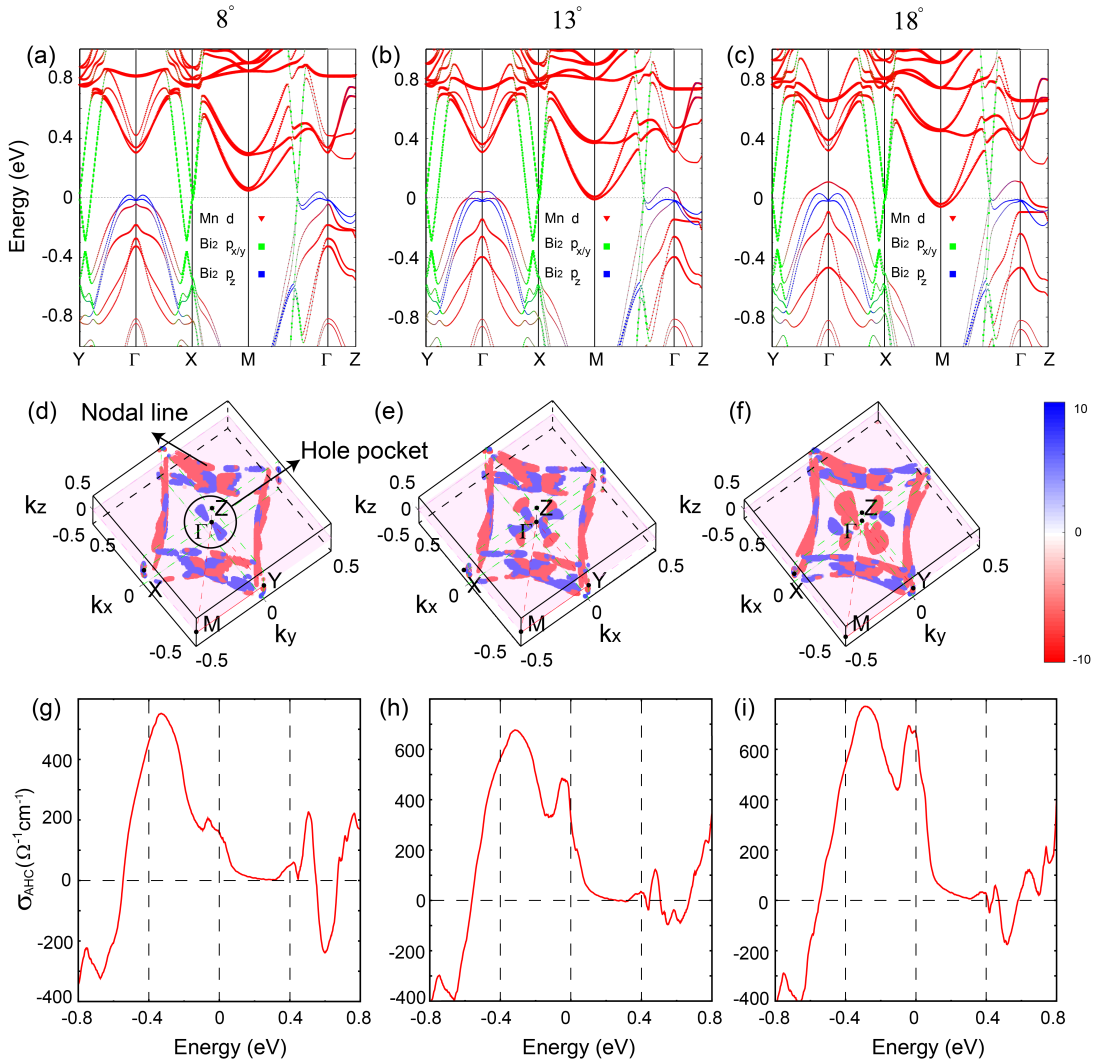


FIG. 3: (color online) (a)-(c) The band structures with spin canted C-type AFM states at 8° , 13° and 18° canting angles, respectively. The orbital characters of bands are represented by different colors. (d)-(f) show the local momentum distribution of Berry curvature in the BZ σ_{total} at 8° , 13° and 18° canting angles, respectively. (g)-(i) The energy-dependent AHC σ_{AHC} at 8° , 13° and 18° canting angles.

To further explore the effect of holes and electrons doping on AHC σ_{AHC} , Fig.3(d)-(f) show the energy-dependent AHC σ_{AHC} calculated from the Berry curvature at 8° , 13° and 18° canting angles. When the Fermi level is at the charge neutral points, the AHC σ_{AHC} are 110, 230 and $470 \Omega^{-1}\text{cm}^{-1}$ respectively, indicating that the AHC keep growing as canting angle increases. At 13° and 18° canting angles, a peak in σ_{AHC} appears around Fermi level, shown in Fig.3(e) and (f). Additionally, it is clear that doping electrons can reduce AHC while doping holes strengthen AHC.

In order to consider the effect of correlation effect on AHC in the canted C-type AFM order, Fig.4 shows band structures and AHC with the effective on-site Coulomb U being 2 eV and 4 eV for Mn d orbitals at 18° canting angles in the GGA+ U calculation. The gap between Mn d orbitals (red) increases as U increases, while band structures attributed by intercalated Bi_2 p orbitals (green and blue) remain unchanged, shown in Fig.4(a) and (b). Compared with band structures without U ,

the d-orbital bands with U stay away from Fermi level, and the bands at Fermi level are mainly attributed to the Bi_2 p orbitals. Fig.4(c) and (d) show energy-dependent AHC tensor σ_{AHC} with U being 2 eV and 4 eV for Mn d orbitals at 18° canting angles, and AHC tensors σ_{AHC} with U are small compared with that without U , indicating that the correlation effect can suppress AHC.

Since the spin canting exist in the YbMnBi_2 , we calculate AHC tensors and band structures of YbMnBi_2 at different canting angles. Similar to CaMnBi_2 , the ferromagnetism in the xy plane becomes larger with the increasing of the canting angle, and the hole pocket at Γ point contributed by Mn d orbitals will become larger, which can result in big and negative Berry curvature. Therefore, the AHC σ_{AHC} in the YbMnBi_2 also increases as the canting angle increases. The energy-dependent AHC σ_{AHC} is also calculated at different canting angles, and we find that doping electrons can suppress AHC while doping holes strengthen AHC.

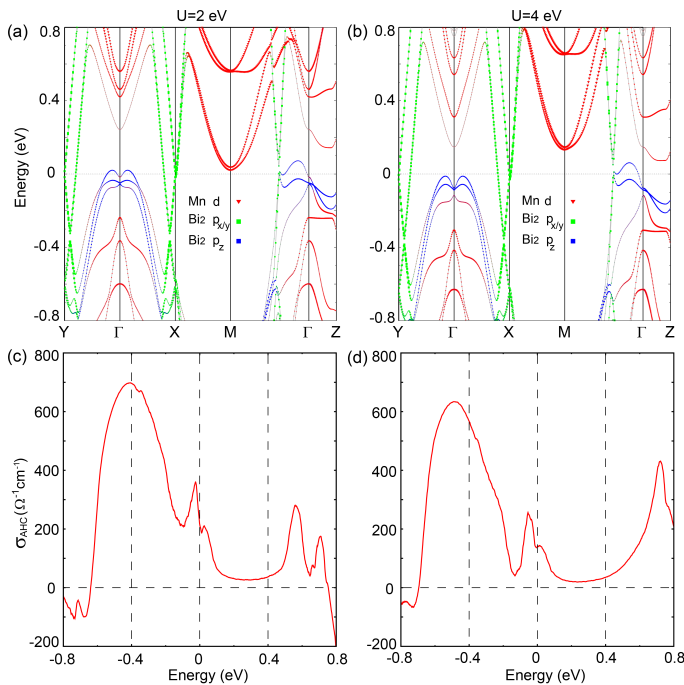


FIG. 4: (color online) The band structures and corresponding energy-dependent AHC tensor σ_{AHC} with the effective on-site Coulomb U being (a,c) 2 eV and (b,d) 4 eV for Mn d orbitals at 18° canting angles in the GGA+ U calculation.

V. CONCLUSION

In summary, the AHE in the layered ternary materials $AMnBi_2$ ($A=Ca$ and Yb) with spin canted C-type antiferromagnetic order can be studied based on first-principles calculations and symmetry analysis. By taking the canting along the $(1,1,0)$ direction, the magnetic space group is $m'm2'$, and only $\sigma_{xz/yz}$ in the AHC tensors are non-zero due to mirror symmetry. We find that the AHC σ_{AHC} always keep growing with the canting angle increasing, and doping electrons can reduce AHC while doping holes strengthen AHC. The correlation effect from Mn d orbitals is considered, and can suppress AHC. This work provides an effective design strategy and corresponding materials to have strong AHE.

VI. ACKNOWLEDGMENTS

We thank Yu Pan for helpful discussions. This work was financially supported by the ERC Advanced Grant No. 291472 'Idea Heusler', ERC Advanced Grant No. 742068 'TOP-MAT', SKYTOP with grant No. 824123, ASPIN with grant No. 766566, DAAD grant No. 57559136. Some of our calculations were carried out on the Cobra cluster of MPCDF, Max Planck society.

* Electronic address: Corresponding: ysun@cpfs.mpg.de

- ¹ Nagaosa, N., Sinova, J., Onoda, S., MacDonald, A. H. Ong, N. P. Rev. Mod. Phys. 82, 1959-2007 (2010).
- ² Z. Fang, N. Nagaosa, K. S. Takahashi, A. Asamitsu, R. Mathieu, T. Ogasawara, H. Yamada, M. Kawasaki, Y. Tokura, and K. Terakura, Science 302, 92 (2003).
- ³ Haldane, F. D. M, Phys. Rev. Lett. 93, 206602 (2004).
- ⁴ Xiao, D., Chang, M. C. Niu, Q. Berry phase effects on electronic properties. Rev. Mod. Phys. 82, 1959-2007 (2010).
- ⁵ Enke Liu, Yan Sun, Nitesh Kumar, Lukas Muechler, Aili Sun, Lin Jiao, Shuo-Ying Yang, Defa Liu, Aiji Liang, Qiunan Xu, Johannes Kroder, Vicky Su, Horst Borrmann, Chandra Shekhar, Zhaosheng Wang, Chuanying Xi, Wenhong Wang, Walter Schnelle, Steffen Wirth, Yulin Chen, Sebastian T. B. Goennenwein and Claudia Felser, Nat. Phys. 14, 1125-1131 (2018).
- ⁶ Wang, Q., Xu, Y., Lou, R. et al, Nat Commun 9, 3681 (2018).
- ⁷ Qiunan Xu, Enke Liu, Wujun Shi, Lukas Muechler, Jacob Gayles, Claudia Felser, and Yan Sun, Phys. Rev. B 97, 235416 (2018)
- ⁸ Cheng Tan, Jinhwan Lee, Soon-Gil Jung, Tuson Park, Sultan Albarakati, James Partridge, Matthew R. Field, Dougal G. McCulloch, Lan Wang, and Changu Lee, Nat Commun 9, 1554 (2018)
- ⁹ Kyoo Kim, Junho Seo, Eunwoo Lee, K.-T. Ko, B. S. Kim, Bo Gyu Jang, Jong Mok Ok, Jinwon Lee, Youn Jung Jo, Woun Kang, Ji Hoon Shim, C. Kim, Han Woong Yeom, Byung Il Min, Bohm-Jung Yang and Jun Sung Kim, Nature Mater 17, 794-799 (2018).
- ¹⁰ Guin, S.N., Manna, K., Noky, J. et al, NPG Asia Mater 11, 16 (2019)
- ¹¹ Peigang Li, Jahyun Koo, Wei Ning, Jinguo Li, Leixin Miao, Lujin Min, Yanglin Zhu, Yu Wang, Nasim Alem, Chao-Xing Liu, Zhiqiang Mao and Binghai Yan, Nat Commun 11, 3476 (2020).

- ¹² J. Kubler and C. Felser, EPL, 114 (2016) 47005
- ¹³ Jonathan Noky, Qiunan Xu, Claudia Felser, and Yan Sun, Phys. Rev. B 99, 165117 (2019)
- ¹⁴ Kaustuv Manna, Yan Sun, Lukas Muechler, Jurgen Kubler and Claudia Felser, Nat Rev Mater 3, 244-256 (2018).
- ¹⁵ Kaustuv Manna, Lukas Muechler, Ting-Hui Kao, Rolf Stinshoff, Yang Zhang, Johannes Gooth, Nitesh Kumar, Guido Kreiner, Klaus Koepf, Roberto Car, Jurgen Kubler, Gerhard H. Fecher, Chandra Shekhar, Yan Sun, and Claudia Felser, Phys. Rev. X 8, 041045 (2018)
- ¹⁶ R. Shindou, N. Nagaosa, Phys. Rev. Lett. 87, 116801 (2001).
- ¹⁷ H. Chen, Q. Niu, A. H. MacDonald, Phys. Rev. Lett. 112, 017205 (2014).
- ¹⁸ J. Kubler, C. Felser, Europhys. Lett. 108, 67001 (2014).
- ¹⁹ S. Nakatsuji, N. Kiyohara, and T. Higo, Nature (London) 527, 212 (2015).
- ²⁰ A. K. Nayak, J. E. Fischer, Y. Sun, B. Yan, J. Karel, A. C. Komarek, C. Shekhar, N. Kumar, W. Schnelle, J. Kubler, C. Felser, and S. S. P. Parkin, Sci. Adv. 2, e1501870 (2016).
- ²¹ Y. Zhang, Y. Sun, H. Yang, J. zelezny, S. P. P. Parkin, C. Felser, and B. Yan, Phys. Rev. B 95, 075128 (2017).
- ²² R. D. dos Reis, M. Ghorbani Zavareh, M. O. Ajeesh, L. O. Kutevlak, A. S. Sukhanov, Sanjay Singh, J. Noky, Y. Sun, J. E. Fischer, K. Manna, C. Felser, and M. Nicklas, Phys. Rev. Mater. 4, 051401(R)(2020)
- ²³ Wujun Shi, Lukas Muechler, Kaustuv Manna, Yang Zhang, Klaus Koepf, Roberto Car, Jeroen van den Brink, Claudia Felser, and Yan Sun, Phys. Rev. B 97, 060406(R)(2018)
- ²⁴ Zexin Feng, Xiaorong Zhou, Libor mejkal, Lei Wu, Zengwei Zhu, Huixin Guo, Rafael Gonzalez-Hernandez, Xiaoning Wang, Han

- Yan, Peixin Qin, Xin Zhang, Haojiang Wu, Hongyu Chen, Chengbao Jiang, Michael Coey, Jairo Sinova, Toma Jungwirth, Zhiqi Liu, arXiv:2002.08712
- ²⁵ J. B. He, D. M. Wang, and G. F. Chen, *Appl. Phys. Lett.* **100**, 112405 (2012)
- ²⁶ A. Wang, D. Graf, L. Wu, K. Wang, E. Bozin, Y. Zhu, and C. Petrovic, *Phys. Rev. B* **94**, 125118 (2016).
- ²⁷ A. Zhang, C. Liu, C. Yi, G. Zhao, T. L. Xia, J. Ji, Y. Shi, R. Yu, X. Wang, C. Chen, and Q. Zhang, *Nat. Commun.* **7**, 13833 (2016).
- ²⁸ Ziyang Qiu, Congcong Le, Yaomin Dai, Bing Xu, J. B. He, Run Yang, Genfu Chen, Jiangping Hu, and Xianggang Qiu, *Phys. Rev. B* **98**, 115151 (2018)
- ²⁹ Ziyang Qiu, Congcong Le, Zhiyu Liao, Bing Xu, Run Yang, Jiangping Hu, Yaomin Dai, and Xianggang Qiu, *Phys. Rev. B* **100**, 125136 (2019)
- ³⁰ Sergey Borisenko, Daniil Evtushinsky, Quinn Gibson, Alexander Yaresko, Klaus Koepernik, Timur Kim, Mazhar Ali, Jeroen van den Brink, Moritz Hoesch, Alexander Fedorov, Erik Haubold, Yevhen Kushnirenko, Ivan Soldatov, Rudolf Schafer, Robert J. Cava, *Nature Commun.* **10**, 3424 (2019).
- ³¹ R. Yang, M. Corasaniti, C. C. Le, Z. Y. Liao, A. F. Wang, Q. Du, C. Petrovic, X. G. Qiu, J. P. Hu, and L. Degiorgi, *Phys. Rev. Lett.* **124**, 137201 (2020)
- ³² G. Kresse and J. Hafner, *Phys. Rev. B* **47**, 558 (1993).
- ³³ G. Kresse and J. Furthmuller, *Comput. Mater. Sci.* **6**, 15 (1996).
- ³⁴ G. Kresse and J. Furthmuller, *Phys. Rev. B* **54**, 11169 (1996).
- ³⁵ H. J. Monkhorst and J. Pack, *Phys. Rev. B* **13**, 5188 (1976).
- ³⁶ J. R. Yates, X. Wang, D. Vanderbilt, and I. Souza, *Phys. Rev. B* **75**, 195121 (2007)
- ³⁷ Xianxin Wu, Shengshan Qin, Yi Liang, Heng Fan, and Jiangping Hu, *Phys. Rev. B* **93**, 115129 (2016).